Al-Furat Journal of Innovations in Electronics and Computer Engineering (FJIECE)
ISSN -2708-3985

Performance Evaluation of LDPC-Coded SISO-OFDM Adaptive Modulation and Coding under Rayleigh/Rician Fading and Power Amplifier Nonlinearity

Sajad D. Al-Akash[1*], Ameer H. Ali[2]

[1]Department of Communications Engineering Techniques, Engineering Technical College/Najaf, Al-Furat Al-Awsat Technical University, Najaf, 31001, Iraq. E-mail: sajad.alakash.ms2@student.atu.edu.iq

[2]Najaf Technical Institute, Al-Furat Al-Awsat Technical University, Najaf, 31001, Iraq. E-mail: inj.ame7@atu.edu.iq

Article's Information

Received: 03.06.2026
Accepted: 26.08.2026
Published: 07.10.2026

Keywords:
Adaptive modulation and coding (AMC),
SISO-OFDM,
LDPC coding,
Rayleigh fading,
Rician fading,
Rapp power amplifier,
BER, BLER, goodput.

Abstract

In this paper, a controlled link-level evaluation of a manually decoded low-density parity-check (LDPC)-coded single-input single-output orthogonal frequency-division multiplexing (SISO-OFDM) system with adaptive modulation and coding (AMC) is provided in two frequency-selective fading environments: Rayleigh and Rician fading, with and without a memoryless Rapp power amplifier (PA). The contribution is a fading law-based, repeatable estimation of the shift of the BER calibrated modulation and coding scheme (MCS) activation thresholds as a result of the transmitter nonlinearity, using the same physical layer decoder curves for calibration and evaluating the AMC in the presence of delayed/noisy feedback. The final study is conducted using a SNR range of 0-39 dB in 0.25 dB steps, a target for BER of 10-3, confirmation (2 consecutive points), an activation margin of 0.25 dB, a number of Monte-Carlo frames of 400-800 per fixed-MCS/step and a Doppler-correlated AMC trace of 5000 frames. The activation threshold At 256-QAM, R=2/3, Rician fading lowers the activation threshold from 37.00 to 30.25 dB without PA and from 38.25 to 31.25 dB with PA. The PA changes this threshold by 1.25 dB when it is used in Rayleigh fading and by 1.00 dB when it is used in Rician fading at 7 dB input back-off. At 39 dB, AMC goodput is 41.73, 39.33, 44.80, and 44.75 Mbit/s for Rayleigh/no-PA, Rayleigh/PA, Rician/no-PA, and Rician/PA, respectively. The observed results indicate that the PA penalty at this back-off is manifested primarily as a delay in the activation of high-order MCS, instead of the loss of the highest MCS at the higher end of simulated SNR range.

https://doi.org/10.46649/fjiece.v5.2.3a.7.10.2026

*Corresponding author: sajad.alakash.ms2@student.atu.edu.iq

1. INTRODUCTION

In the field of broadband wireless links, orthogonal frequency-division multiplexing (OFDM) is widely used, and a cyclic prefix (CP) can be used to convert the frequency-selective multipath channel into a set of approximately flat subchannels in the frequency domain to support low complexity frequency domain equalization [1]-[4]. AMC is used with OFDM; it changes the modulation and coding scheme (MCS) based

ATU-FJIECE, Volume: 5, Issue: 2, 10, 7, 2026, © 2020 FJIECE, All Rights Reserved

on link quality. For Long-Term Evolution (LTE) and Fifth-Generation New Radio (5G NR), channel-quality feedback, MCS selection and target error-rate requirements [5] and [6] are used for related link-adaptation mechanisms.

Additionally, a practical OFDM transmitter has a high peak-to-average power ratio (PAPR) and is susceptible to the radio-frequency power-amplifier (PA) nonlinearity. A power efficient operation is possible by operating the PA closer to saturation, but this causes compression and non-linear distortion in-band that reduces the density of quadrature amplitude modulation (QAM) constellations and may shift the SNR region for a particular reliable MCS [7]-[10]. Thus, the evaluation of AMC behavior should be done in conjunction with propagation fading, transmitter nonlinearity, and not only with an ideal linear front end. The existing literature includes OFDM over Rayleigh/Rician fading [13], [14], channel coding [20]-[23], link adaptation [15], [17], [24]-[28], PA behavioral modeling [7]-[10], digital predistortion [8], [29], [34] and PAPR reduction [30], receiver-side compensation techniques [31], [32] and PA-aware multi-antenna processing techniques [33], [34]. The gap to be filled here is more limited: A controlled threshold level comparison where the same manually decoded LDPC-coded SISO-OFDM chain is calibrated and evaluated under four matched conditions - Rayleigh/Rician fading and PA disabled/enabled. This work does not propose a new LDPC coding scheme, nor does it propose a new PA model. The contribution is a repeatable integration study to quantify the movement of BER-derived MCS operating boundaries and the resulting payload goodput as a result of the contribution of the channel law and PA state.

The specific contributions are: (i) fixed-MCS calibration based on the actual iterative LDPC decoder on a fine SNR grid of 0.25 dB; (ii) a transparent BER-threshold rule based on 2 consecutive qualifying points with a 0.25 dB activation margin; (iii) a dynamic AMC evaluation on a Doppler-correlated channel-power trace with a 2-frame delayed and 0.25 dB noisy feedback; and (iv) a dedicated quantitative comparison of activation threshold, BER, block-error rate (BLER), and goodput for all four fading/PA cases. The final implementation does not explicitly use the effective-SINR mapping based on mutual-information (MIESM); it is explained clearly that this method is different from other approaches for link-to-system mapping [25].

The remainder of the paper is organized as follows. Section 2 summarizes related work. Section 3 describes the implemented physical-layer calibration and AMC method. Section 4 gives the complete simulation setup and assumptions. Section 5 discusses the final results. Section 6 concludes the paper.

2. RELATED WORK

The foundation of this work is provided by the study of digital communications, fading channels, OFDM, and MIMO-OFDM, which outline the performance of a multicarrier link with multipath propagation and lay the groundwork for one-tap frequency domain reception [1]-[4]. The dependence of the error probability on the fading statistics and modulation order is also highlighted in the Rayleigh and Rician OFDM studies [13, 14]. The implementation of the receiver and adaptation of the transmitter in a MIMO-OFDM and related coded multicarrier systems have also been studied [15]-[17].

The quality and timely availability of link information are crucial to AMC reliability. Channel-estimation studies have found that estimation error impacts equalization and link adaptation [18] and [19] and recent work has focused on channel coding, high throughput LDPC decoding, channel-quality-indicator (CQI) prediction, outer-loop link adaptation, enriched hybrid automatic repeat request (HARQ) feedback, and learning-based MCS selection [20]-[24], [26]-[28]. Even for the fixed-MCS equalizer (which is assumed to have perfect CSI in the present paper), the AMC control metric is made to be explicitly delayed from CSI and noisy.

The PA literature covers the field of behavioral modelling and predistortion [8, 29], PAPR reduction [30], PA-aware massive-MIMO processing [33] and beamforming-transmitter predistortion [34]. Unlike this study, a new method for determining PA compensation is not suggested. It identifies the link-adaptation

Al-Furat Journal of Innovations in Electronics and Computer Engineering (FJIECE)
ISSN -2708-3985

consequence of a given memoryless Rapp AM/AM model by observing the variation of calibrated MCS thresholds when the PA is turned on. This is the key differentiation when compared to the studies cited above which are PA-focused. Other related signal-processing contributions in terms of coded multi-carrier and frequency domain signal processing by Ameer H. Ali are mentioned in [11] and [12].

3. SYSTEM MODEL AND AMC METHODOLOGY

3.1. Implemented two-stage link

There are two phases of the final implementation (see Fig. 1). Stage A: Full physical-layer simulation of MCS, with a determinant LDPC code determined by the manual, QAM mapping, bits interleaved and active OFDM subcarriers, inverse fast Fourier transform (IFFT) and CP protecting. Before the six-tap Rayleigh or Rician fading channel and additive white Gaussian noise (AWGN), there is an optional memoryless Rapp PA. The receiver strips the CP, applies a fast Fourier transform (FFT), performs one-tap SISO minimum-mean-square-error (MMSE) equalization, applies max-log log-likelihood ratios (LLRs), deinterleaves and runs scaled Min-Sum LDPC decoding. The information bits that are successfully delivered are added to BER, BLER.
Stage B is not a second full waveform simulation, but instead an abstraction of an AMC link calibrated. The fixed-MCS curves give the MCS activation thresholds and the BER/BLER/goodput lookup behaviour of the curves are derived from them. The current SNR is then computed from a temporally correlated wideband channel-power trace, the highest eligible MCS is selected by the delayed/noisy feedback, and the performance of the selected MCS is interpolated from the performance curve for a fixed-MCS. This structure is compatible with the actual simulation code and does not suggest non-existent processing blocks such as no CRC attachment, bit-exact rate matching for 5G-NR, pilot-based channel estimator, MIESM or mutual-information mapping.

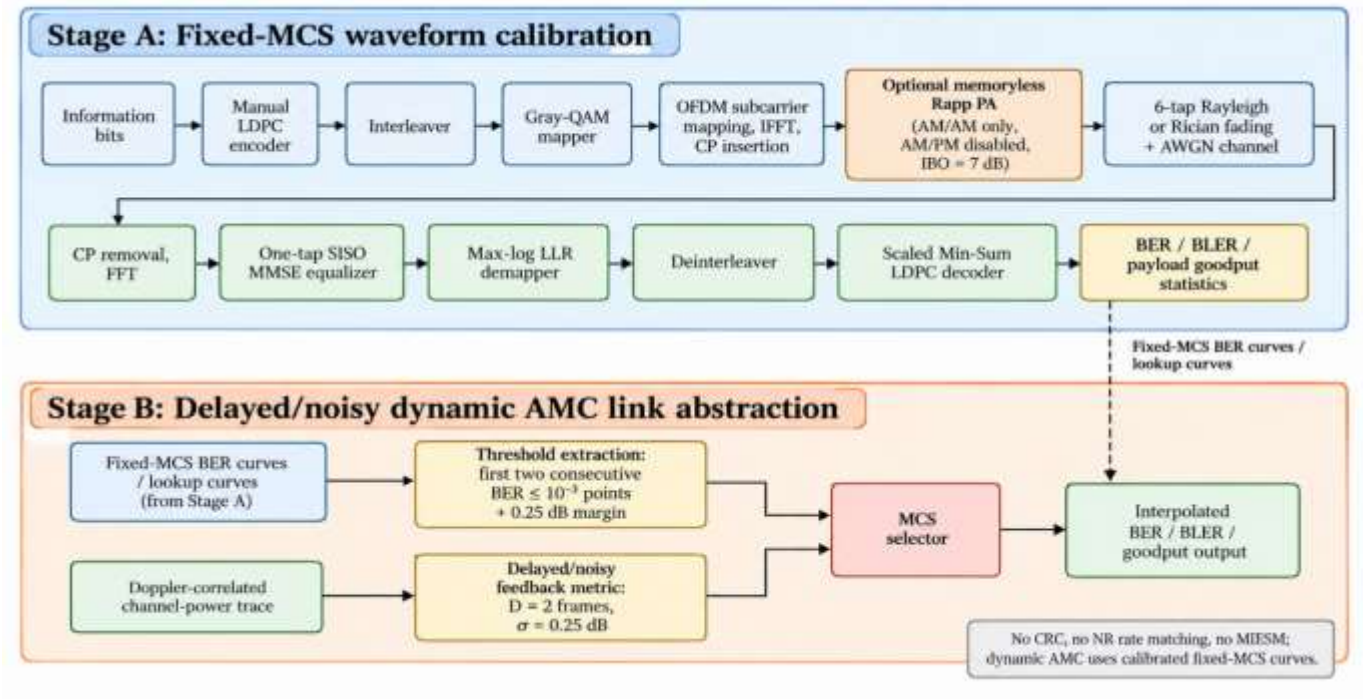

Fig. 1. Implemented two-stage LDPC-coded SISO-OFDM AMC framework: fixed-MCS waveform calibration and delayed/noisy dynamic AMC link abstraction.

Al-Furat Journal of Innovations in Electronics and Computer Engineering (FJIECE)
ISSN -2708-3985

3.2. MCS, coding, and OFDM processing

Seven MCS modes are evaluated: QPSK with R=1/2 and 2/3; 16-QAM with R=1/2 and 2/3; 64-QAM with R=1/2 and 2/3; and 256-QAM with R=2/3. For modulation order Q_m bits/symbol and code rate R_m, the nominal coded spectral-efficiency index is

$$\eta_m = Q_m R_m [\text{ bit /s/Hz}] \quad (1)$$

The manual LDPC code has a fixed codeword length n=600 bits. Rate 1/2 uses k=300 information bits and rate 2/3 uses k=400 information bits. The parity-check matrix is deterministic and systematic, H=[A|B], with information-side effective column weight three and a lower-bidiagonal parity part B. The decoder uses a flooding-style scaled Min-Sum schedule, scale factor 0.80, LLR clipping at 25, and at most 10 iterations. A block that still contains information-bit errors after decoding is counted as a BLER event. This is a thesis-level manual LDPC implementation, not a bit-exact 3GPP NR LDPC chain.
Each frame contains 600 active subcarriers and 14 OFDM symbols. With no pilots or control-resource puncturing, the number of information bits per simulated frame depends on the MCS and ranges from 8400 bits for QPSK R=1/2 to 44800 bits for 256-QAM R=2/3.

3.3. Fading channel, PA model, and receiver

The six-tap power-delay profile (PDP) is exponentially decaying. With decay factor a=0.65, the normalized tap powers are

$$p_\ell = \frac{0.65^\ell}{\sum_{i=0}^{5} 0.65^i}, \ell = 0, \ldots, 5 \quad (2)$$

Numerically, the six normalized powers are [0.3785, 0.2461, 0.1599, 0.1040, 0.0676, 0.0439]. For Rayleigh fading, each tap is a zero-mean circular complex Gaussian variable scaled by √p_l. For Rician fading with K=6 dB, the deterministic line-of-sight (LOS) component is placed on the first tap and combined with the normalized non-LOS component as

$$\mathbf{h} = \sqrt{\frac{K}{K+1}}\mathbf{h}_{\text{LOS}} + \sqrt{\frac{1}{K+1}}\mathbf{h}_{\text{NLOS}} \quad (3)$$

which gives E{Σ_l |h_l|²}=1 without normalizing every realization to unit instantaneous power. During a fixed-MCS physical-layer frame the tap vector is held constant across the 14 OFDM symbols and a new realization is generated for the next Monte-Carlo frame. The dynamic AMC trace, in contrast, uses a first-order Jakes-correlated tap process across frames.
When enabled, the PA is the memoryless Rapp AM/AM model with smoothness parameter p=2 and input back-off (IBO) of 7 dB. AM/PM conversion is disabled in the final configuration. For input x and saturation amplitude A_sat determined from the frame-average input power,

$$y_{\text{PA}} = \frac{x}{[1+(|x|/A_{\text{sat}})^{2p}]^{1/(2p)}} \quad (4)$$

Al-Furat Journal of Innovations in Electronics and Computer Engineering (FJIECE)
ISSN -2708-3985

The memoryless model is used deliberately to isolate static nonlinear compression in the AMC study. Wideband memory effects are outside the present scope and are identified as a future extension; this limitation should be kept in mind when extrapolating the results to measured RF hardware [7]-[9].
The fixed-MCS receiver assumes perfect knowledge of the channel frequency response, so its one-tap MMSE equalizer is an upper-bound baseline for the channel-estimation part of the receiver. In the PA case, the framewise linear PA gain α is used to define the effective linear channel, while the residual nonlinear component contributes to the demapper variance. No per- subcarrier SINR or SNDR is averaged for AMC, and no mutual-information function is used. The max-log LLR demapper operates directly with the equalized symbol, effective complex gain, and effective variance.

3.4. BER-calibrated thresholds and delayed/noisy AMC

For each channel/PA case, every MCS is first simulated over 0-39 dB in 0.25 dB steps. Let the measured BER of MCS m at grid point γ_i be denoted $BER_m(\gamma_i)$. The raw target crossing is the first grid point for which two consecutive samples satisfy the target BER of 10^-3. The activation threshold used by AMC is

$$\theta_m = \gamma_{m,\,cross} + 0.25\text{dB}, m > 0 \quad (5)$$

where the additional 0.25 dB is a safety margin. The most robust QPSK R=1/2 mode is retained as an always-available fallback; its true BER-target crossing is still reported separately. The reference BLER=0.1 line is used only as a diagnostic in the plots and is not the AMC switching criterion. No bidirectional hysteresis or hold timer is applied; the two-point crossing confirmation and activation margin provide conservative calibration.
For dynamic AMC, user speed is 30 km/h at 3.5 GHz. The maximum Doppler frequency is 97.29 Hz, the OFDM-frame duration is 0.999 ms, the Jakes correlation coefficient between adjacent frames is 0.9089, and the approximate coherence time is 4.35 ms. For average SNR $\bar{\gamma}$, the frame-t feedback metric is

$$\gamma_{fb}[t] = \bar{\gamma} + 10\log_{10}(P_{ch}[t-D]) + e[t-D] \quad (6)$$

where D=2 frames (1.998 ms), Pch is the normalized wideband channel power, and e is zero-mean Gaussian feedback error with 0.25 dB standard deviation. The selected MCS is the highest-efficiency mode whose threshold is not greater than γfb[t]:

$$m[t] = \arg\max_m\{\eta_m : \gamma_{fb}[t] \geq \theta_m\} \quad (7)$$

The current, non-delayed channel SNR is then used to interpolate the fixed-MCS BER, BLER, and goodput curve of the selected mode. Therefore, delay affects the decision, whereas the delivered performance reflects the channel state at transmission time. The dynamic averages are computed over 5000 correlated trace frames at every average-SNR point.

ATU-FJIECE, Volume: 5, Issue: 2, 10, 7, 2026, © 2020 FJIECE, All Rights Reserved

Al-Furat Journal of Innovations in Electronics and Computer Engineering (FJIECE)
ISSN -2708-3985

Algorithm 1 BER-threshold extraction and dynamic AMC selection

1. *for each MCS and each SNR grid point do*
2. *Run the full LDPC-coded OFDM physical layer.*
3. *Measure BER, BLER, and goodput.*
4. *end for*
5. *for each non-fallback MCS do*
6. *Find the first two consecutive SNR samples with BER≤10^(-3).*
7. *Add 0.25 dB to form the activation threshold.*
8. *end for*
9. *Keep QPSK R=1/2 always available as the fallback mode.*
10. *Generate a 5000-frame Doppler-correlated channel-power trace and a 0.25 dB-rms feedback-error trace.*
11. *for each AMC frame t do*
12. *Form the delayed metric from frame t-2.*
13. *Select the highest-efficiency MCS whose thresh-old is met.*
14. *Evaluate the selected mode at the current channel SNR by interpolating its calibrated fixed-MCS curves.*
15. *end for*
16. *Average BER, BLER, goodput, and selected-MCS statistics over the trace.*

3.5. Goodput definition

The reported rate is payload goodput, not a complete system throughput including all protocol overheads. A successfully decoded LDPC block contributes its k information bits; an erroneous block contributes zero delivered bits. With frame duration Tf,

$$G = \frac{N_{\text{delivered}}}{T_f} \tag{8}$$

The frame duration includes the CP. HARQ retransmissions, pilot/control overhead, scheduling overhead, and higher-layer signaling are not simulated. Consequently, the reported goodput is an idealized no-HARQ link-level payload rate and should not be interpreted as end-to-end user throughput.

4. SIMULATION SETUP AND ASSUMPTIONS

All numerical results and figures in this paper have been obtained from the final configuration listed in table I. The SNR grid, common random number technique and the stopping rule based on the confidence were completed prior to runs.The common random number technique, the stopping rule based on the confidence and the SNR grid were fixed before final runs. One channel realization is generated independently for each fixed-MCS frame, thus the number of channel realizations for the fixed-MCS/SNR point is equal to the number of frames simulated at that point. The set range is 400-800 frames, but the results from the final files ended at 400-412 frames because the 95% Wilson BER confidence interval went entirely above or below the target 10^{-3}. The dynamic AMC abstraction is based on 5000 pairs of channel power samples correlated at each average-SNR point.

ATU-FJIECE, Volume: 5, Issue: 2, 10, 7, 2026, © 2020 FJIECE, All Rights Reserved

Al-Furat Journal of Innovations in Electronics and Computer Engineering (FJIECE)
ISSN -2708-3985

TABLE I. FINAL SIMULATION PARAMETERS

Parameter	Final value
FFT / active subcarriers / OFDM symbols	1024 / 600 / 14
CP / subcarrier spacing	72 samples / 15 kHz
SNR grid	0-39 dB in 0.25 dB steps
MCS set	QPSK R=1/2,2/3; 16-QAM R=1/2,2/3; 64-QAM R=1/2,2/3; 256-QAM R=2/3
LDPC	n=600; k=300 or 400; column weight 3; scaled Min-Sum 0.80; max 10 iterations
Information bits per frame	8400 to 44800, depending on MCS
Fixed-MCS Monte Carlo	400 minimum, 800 maximum; actual final points 400-412 frames/channel realizations
BER confidence rule	95% Wilson interval relative to BER target 10^{-3}
Channel	6-tap frequency-selective Rayleigh/Rician; exponential PDP decay 0.65; Rician K=6 dB
Fixed-MCS time variation	Block fading within a frame; new realization per Monte-Carlo frame
Dynamic AMC time variation	Jakes-correlated trace; 5000 frames per average-SNR point
Mobility	3.5 GHz, 30 km/h; fD=97.29 Hz; Tc≈4.35 ms
Feedback	D=2 frames (1.998 ms); Gaussian metric error σ=0.25 dB
AMC threshold	BER≤10^{-3} at two consecutive SNR points + 0.25 dB margin
PA	Memoryless Rapp AM/AM; p=2; IBO=7 dB; AM/PM disabled
Randomization	Base seed 20260914; common random numbers enabled
Receiver CSI	Perfect channel response for one-tap MMSE equalization (upper-bound baseline)
Excluded overheads	No HARQ, pilot/control/scheduling overhead, CFO, phase noise, or DPD

5. RESULTS AND DISCUSSION

5.1. Quantitative threshold comparison

Table II focuses directly on the central AMC claim since it spells out the activation thresholds used by the controller. When compared to Rayleigh fading, Rician fading provides an improvement of about 6.0-7.0 dB for each non-fallback MCS activation. The 7 dB-IBO Rapp PA makes the thresholds higher by 0.25 to 0.50 dB for QPSK to 64-QAM and by 1.25 dB (Rayleigh) and/or 1.00 dB (Rician) for 256-QAM R=2/3. The clear PA effect for the last, less severe setting PA is therefore the delay of the higher-order MCS activation, instead of the permanent exclusion of the highest MCS.
Table III cross-checks the final AMC state at 39 dB. All four cases reach 256-QAM R=2/3. The Rayleigh PA case shows a 2.40 Mbit/s (5.76%) goodput reduction relative to Rayleigh/no-PA, whereas the Rician

Al-Furat Journal of Innovations in Electronics and Computer Engineering (FJIECE)
ISSN -2708-3985

PA and no-PA goodputs differ by only 0.05 Mbit/s (0.11%) because both are essentially locked to the highest MCS at this high average SNR. The PA effect remains visible in the activation thresholds and in the mid-SNR transition region

TABLE II. AMC ACTIVATION THRESHOLDS USED BY THE FINAL CONTROLLER (dB)

MCS	Rayleigh no PA	Rayleigh Rapp PA	Rician no PA	Rician Rapp PA
QPSK R=2/3	17.75	18.00	11.75	12.00
16-QAM R=1/2	23.00	23.50	16.50	17.00
16-QAM R=2/3	25.50	26.00	19.00	19.50
64-QAM R=1/2	29.25	29.75	22.75	23.25
64-QAM R=2/3	31.75	32.25	25.00	25.50
256-QAM R=2/3	37.00	38.25	30.25	31.25

TABLE III. FINAL DYNAMIC AMC METRICS AT 39 dB

Case	BER	BLER	Goodput (Mbit/s)	Dominant MCS
Rayleigh, no PA	4.723e-04	8.974e-03	41.73	256-QAM, R=2/3
Rayleigh, Rapp PA	5.236e-04	1.052e-02	39.33	256-QAM, R=2/3
Rician, no PA	3.106e-05	7.613e-04	44.80	256-QAM, R=2/3
Rician, Rapp PA	5.444e-05	1.825e-03	44.75	256-QAM, R=2/3

5.2. Rayleigh fading without PA

The fixed-MCS and AMC BER behaviour is shown separately in Fig. 2. The dynamic BLER is shown in Fig. 3, and the corresponding goodput curves are shown in Fig. 4. The dynamic BLER first falls below the 0.1 reference at 11.75 dB. The AMC BER first falls below 10−3 at 17.0 dB. At 20 dB, QPSK R = 2/3 is dominant, BER is 4.47 × 10−4, BLER is 1.03 × 10−2, and goodput is 10.74 Mbit/s. As higher MCS modes be come eligible, the AMC BER curve shows local upward jumps: these are switching events rather than a loss of monotonic fixed-MCS behaviour. At 30 dB, the dominant mode is 64-QAM R = 1/2 and goodput reaches 24.63 Mbit/s. By 39 dB, 256-QAM R = 2/3 is dominant for 76.1% of the trace and the average

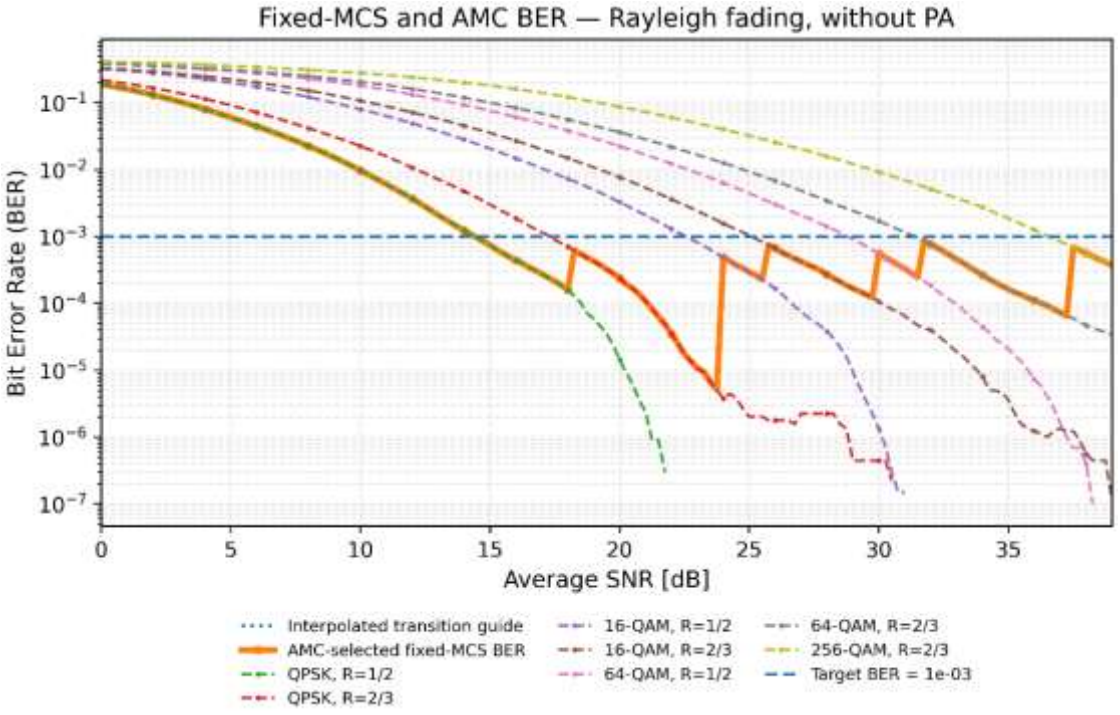

Figure 2: Rayleigh fading without PA: fixed-MCS and AMC BER.

ATU-FJIECE, Volume: 5, Issue: 2, 10, 7, 2026, © 2020 FJIECE, All Rights Reserved

Al-Furat Journal of Innovations in Electronics and Computer Engineering (FJIECE)
ISSN -2708-3985

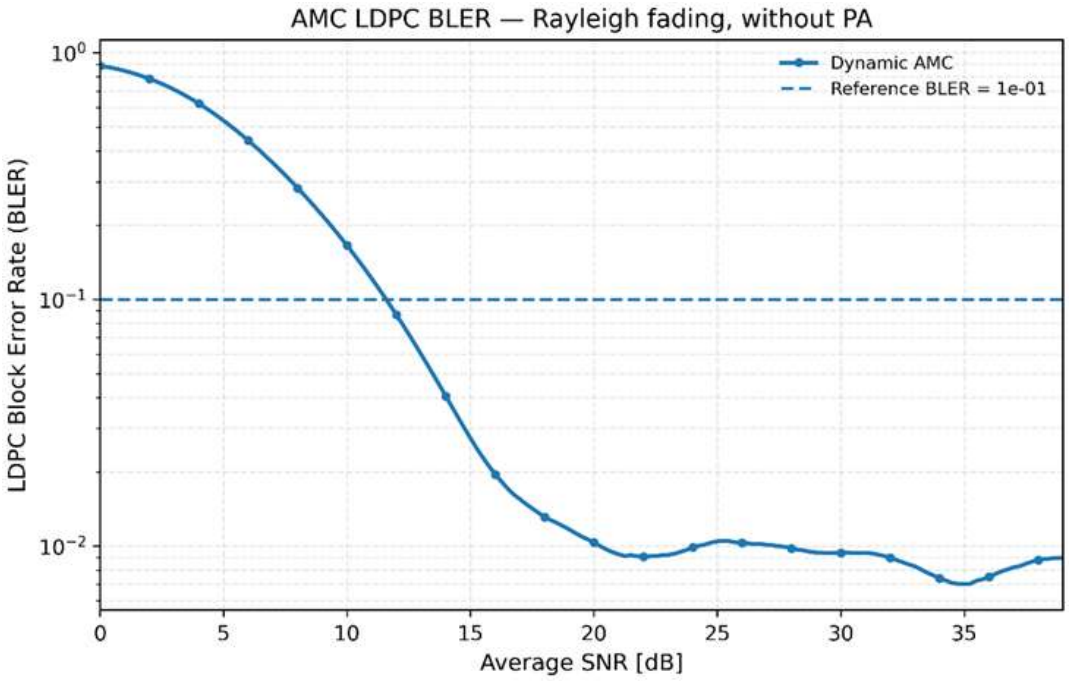

Figure 3: Rayleigh fading without PA: dynamic AMC BLER.

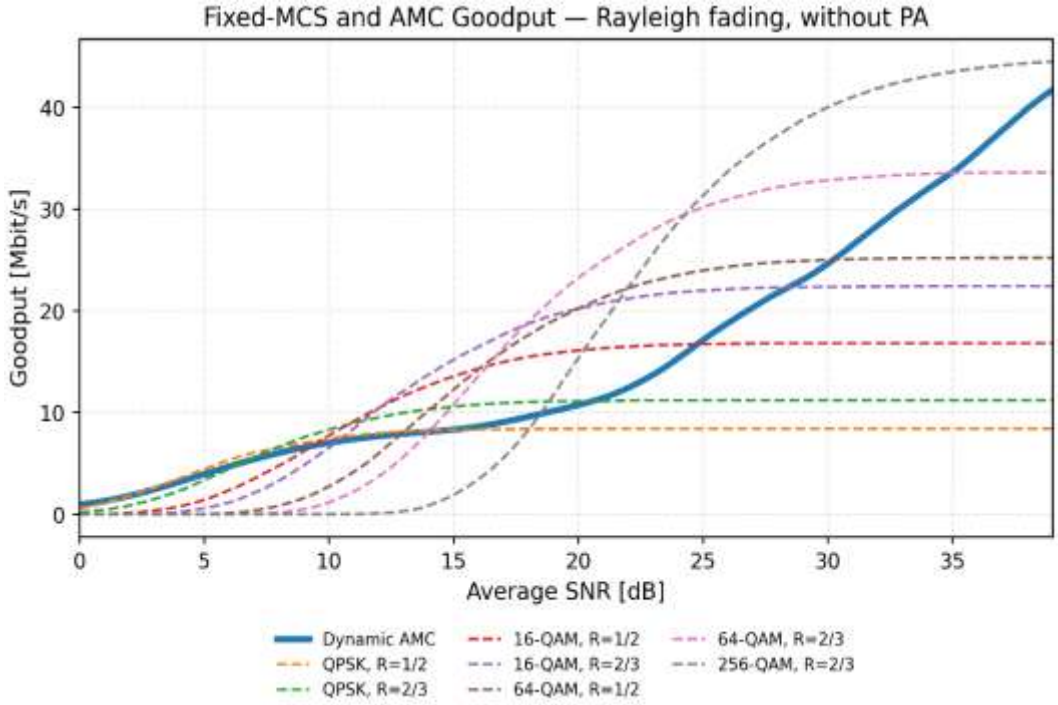

Figure 4: Rayleigh fading without PA: fixed-MCS and AMC goodput.

5.3. Rayleigh fading with Rapp PA

The corresponding BER, BLER, and goodput results are presented separately in Figs. 5–7. With the PA enabled, the BLER=0.1 crossing moves from 11.75 to 12.0 dB and the AMC BER first falls below 10−3 at 17.5 dB. The fixed-MCS threshold table shows a progressively clearer penalty at the highest order: the 256-

ATU-FJIECE, Volume: 5, Issue: 2, 10, 7, 2026, © 2020 FJIECE, All Rights Reserved

Al-Furat Journal of Innovations in Electronics and Computer Engineering (FJIECE)
ISSN -2708-3985

QAM R = 2/3 activation threshold rises from 37.00 to 38.25 dB. At 30 dB the dynamic controller is still dominated by 16-QAM R = 2/3, with 23.79 Mbit/s goodput, whereas the no PA case has already moved into the 64-QAM region. At 39 dB the highest MCS is nevertheless reached; BER is 5.24 × 10−4, BLER is 1.05 × 10−2, and goodput is 39.33 Mbit/s. This indicates that, at 7 dB IBO, the PA causes a measurable but moderate AMC penalty while the highest MCS remains reachable at sufficiently high average SNR.

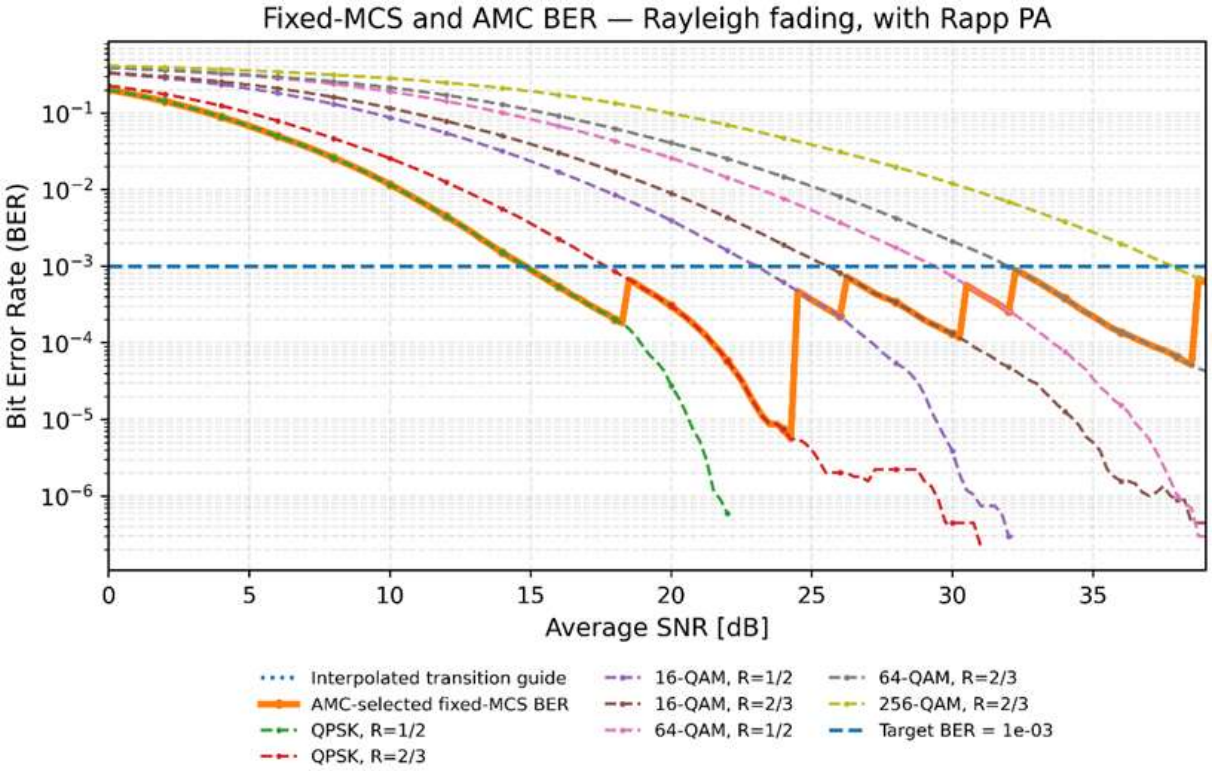

Figure 5: Rayleigh fading with Rapp PA: fixed-MCS and AMC BER.

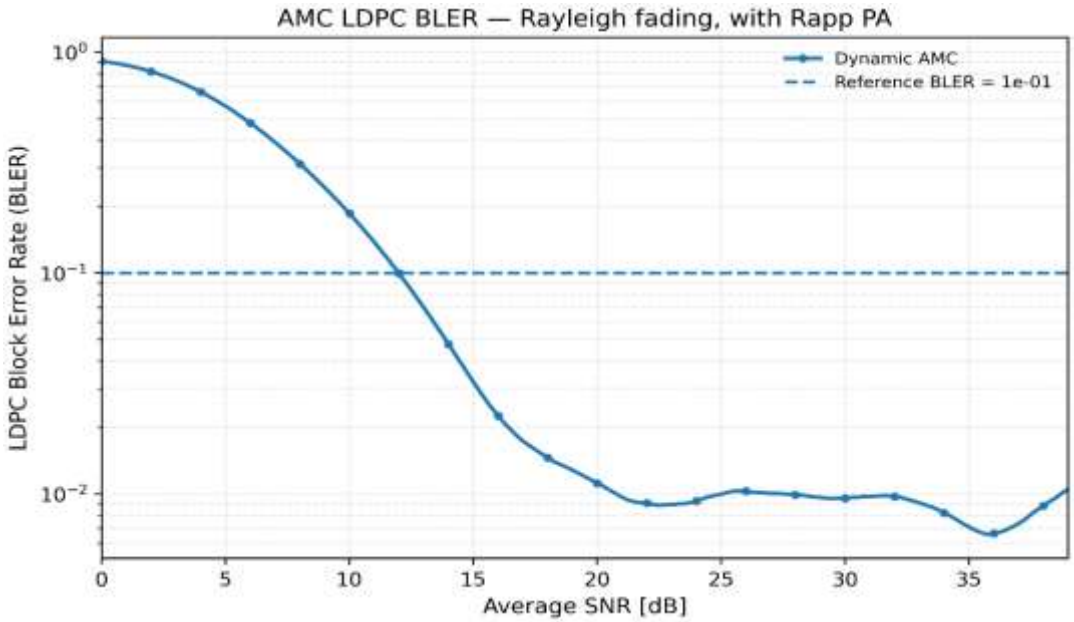

Figure 6: Rayleigh fading with Rapp PA: dynamic AMC BLER.

ATU-FJIECE, Volume: 5, Issue: 2, 10, 7, 2026, © 2020 FJIECE, All Rights Reserved

Al-Furat Journal of Innovations in Electronics and Computer Engineering (FJIECE)
ISSN -2708-3985

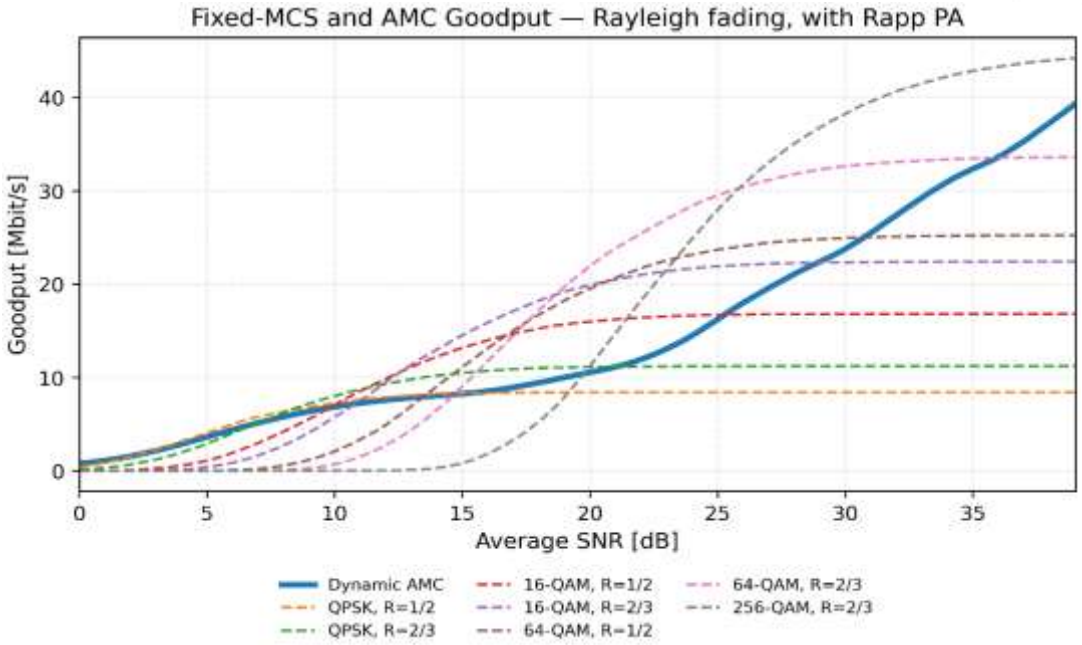

Figure 7: Rayleigh fading with Rapp PA: fixed-MCS and AMC goodput.

5.4. Rician fading without PA

Figures 8–10 show the BER, BLER, and goodput sepa rately. The LOS component produces markedly earlier AMC operation. Dynamic BLER falls below 0.1 at 7.5 dB and AMC BER falls below 10−3 at 11.0 dB. The 256 QAM R =2/3 activation threshold is 30.25 dB, which is 6.75 dB earlier than in Rayleigh/no-PA. Goodput is 20.11 Mbit/s at 20 dB, 37.71 Mbit/s at 30 dB, and 44.80 Mbit/s at 39 dB. At the final SNR point, the highest MCS occupies 99.96% of the AMC trace and BLER is 7.61×10−4, so the achieved goodput is close to the ideal no-error payload ceiling for this numerology.

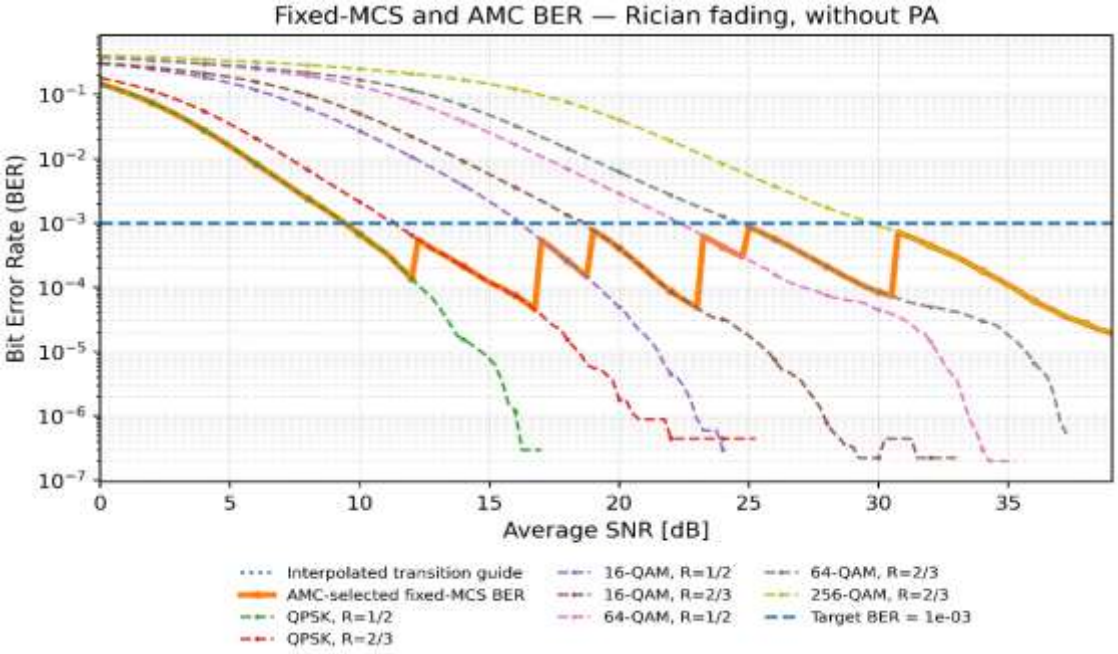

Figure 8: Rician fading without PA: fixed-MCS and AMC BER.

Al-Furat Journal of Innovations in Electronics and Computer Engineering (FJIECE)
ISSN -2708-3985

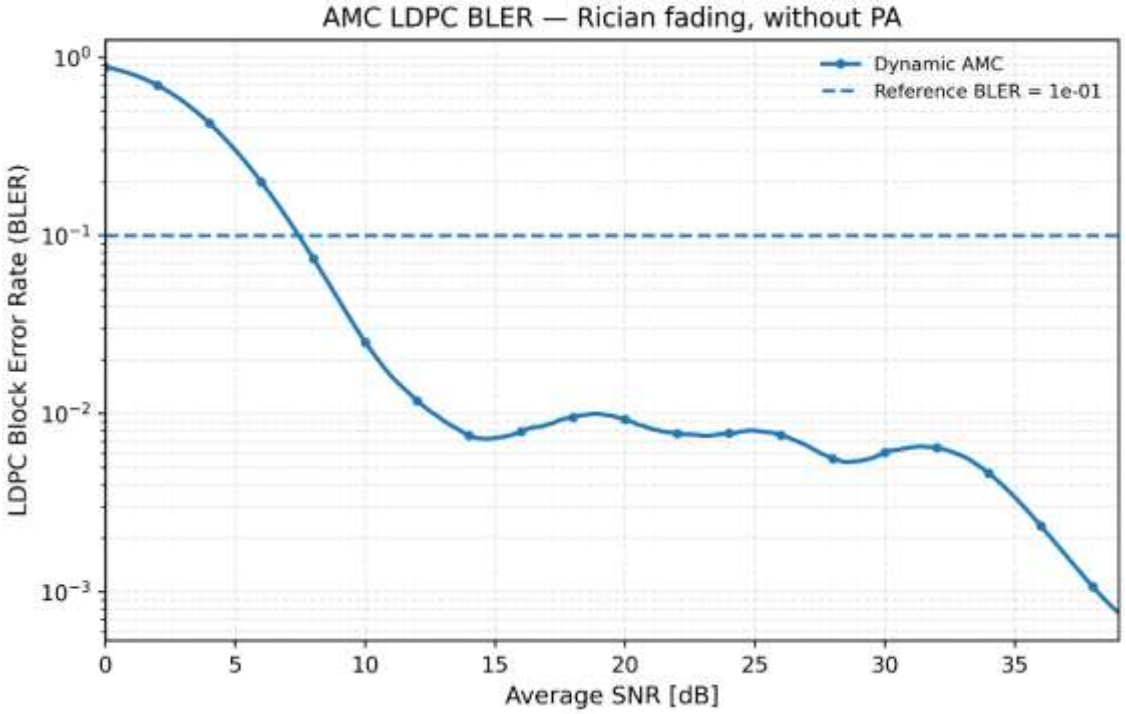

Figure 9: Rician fading without PA: dynamic AMC BLER.

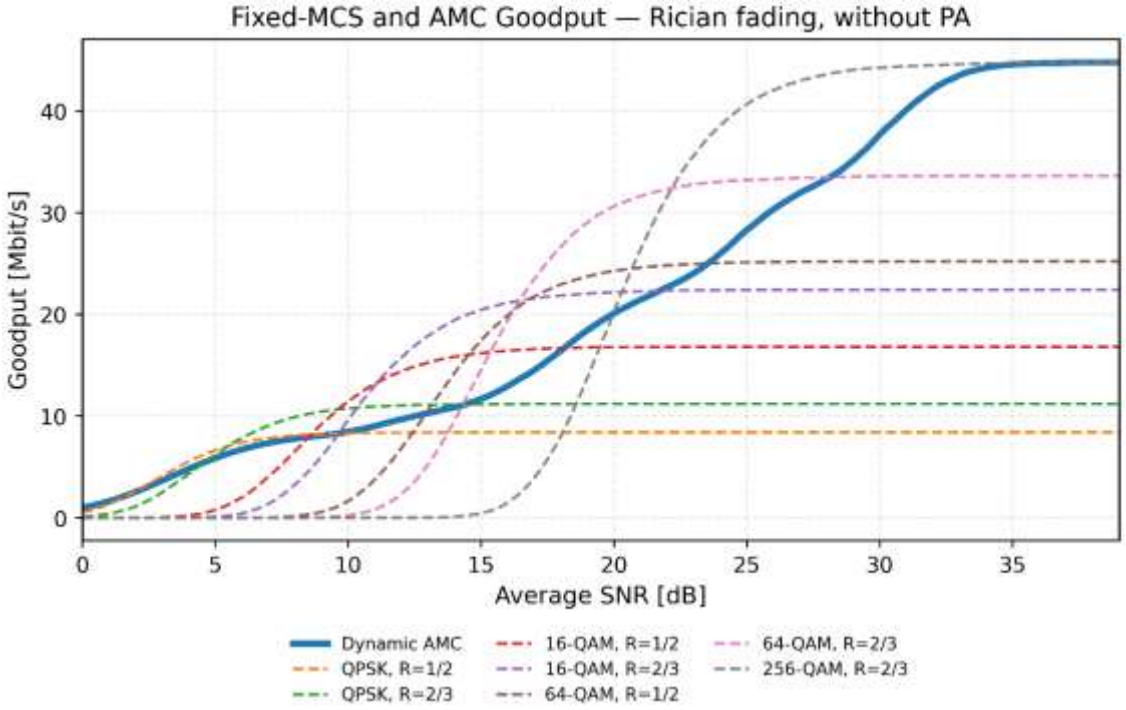

Figure 10: Rician fading without PA: fixed-MCS and AMC goodput.

Al-Furat Journal of Innovations in Electronics and Computer Engineering (FJIECE)
ISSN -2708-3985

5.5. Rician fading with Rapp PA

Figures 11–13 show the corresponding Rician results with PA nonlinearity. The PA shifts the Rician thresh olds upward but does not eliminate the LOS advantage. The BLER reference crossing occurs at 8.0 dB, and AMC BER falls below 10−3 at 11.5 dB. The 256-QAM R=2/3activation threshold is 31.25 dB: 1.00 dB above Rician/no-PA but 7.00 dB below Rayleigh/PA. Goodput is 19.33 Mbit/s at 20 dB, 35.24 Mbit/s at 30 dB, and 44.75 Mbit/s at 39 dB. At 39 dB, BER is 5.44 × 10−5 and BLER is 1.82×10−3. Thus, in the favorable Rician channel, the final 7 dB-IBO PA mainly delays the tran sition to high-order MCS in the mid-SNR region; once the average SNR is sufficiently high, both PA and no PA cases spend essentially the entire trace in 256-QAM R=2/3.

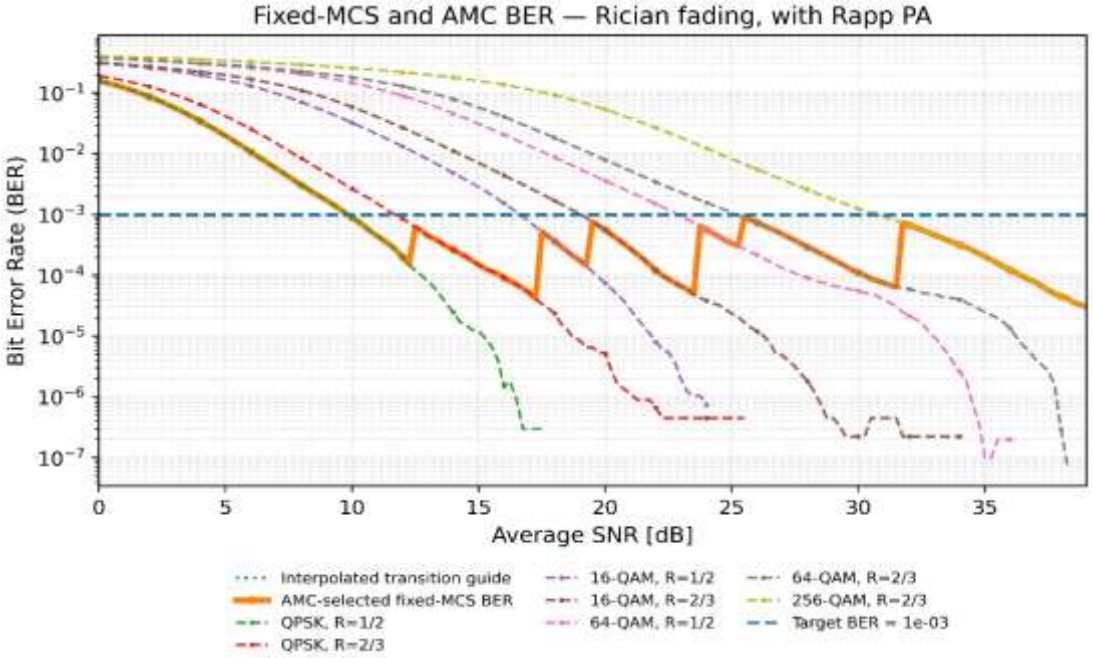

Figure 11: Rician fading with Rapp PA: fixed-MCS and AMC BER.

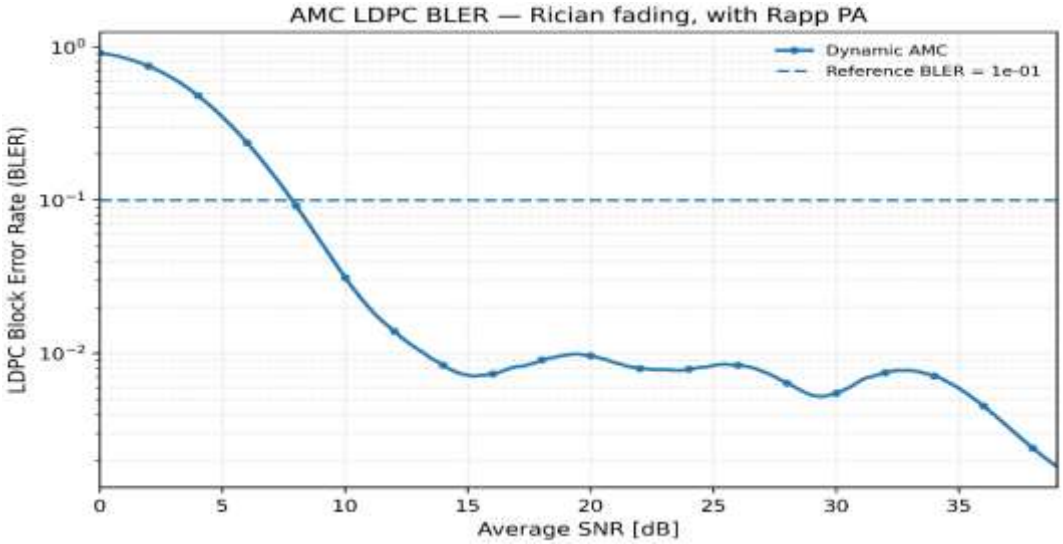

Figure 12: Rician fading with Rapp PA: dynamic AMC BLER.

Al-Furat Journal of Innovations in Electronics and Computer Engineering (FJIECE)
ISSN -2708-3985

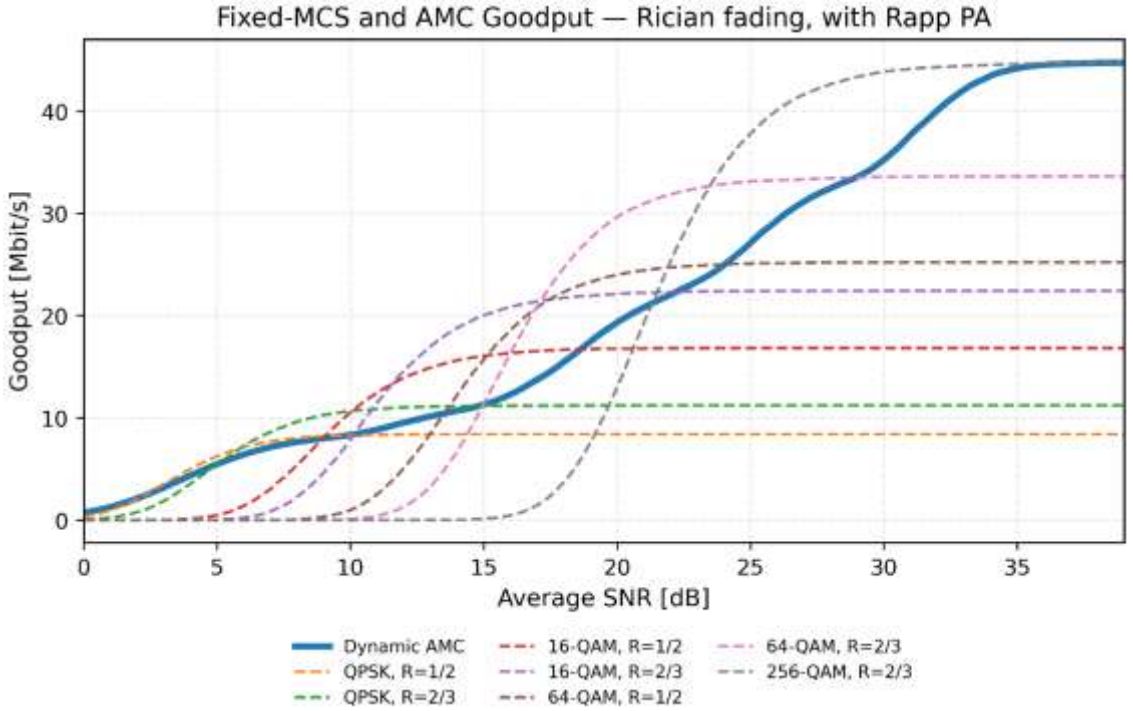

Figure 13: Rician fading with Rapp PA: fixed-MCS and AMC goodput.

5.6. Cross-case observations and statistical interpretation

The final data shows three cross case observations. Rician fading decreases the activation SNR of all upgraded MCS by about 6–7 dB compared to Rayleigh fading because the deterministic component will lessen the impact of deep fading. Second, the 7 dB-IBO Rapp PA shifts all non-fallback thresh olds to the right with the biggest shift caused by 256-QAM R = 2/3. Thirdly, there is no restriction to the use of the highest MCS at 39 dB in the final configuration and the PA effect is most pronounced in the transition region.

The fixed-MCS Monte-Carlo stopping rule is based on the two sided 95% Wilson interval around BER=10−3. Most of the points end at a minimum of 400 frames and only near threshold points need more batches up to 412 frames in the provided final result files. For those small lo cal fluctuations of BER in fixed-MCS, they may stay within finite sample uncertainty, and the extracted tar get crossings are monotonic over MCS order for all four cases and the final goodput curves over MCS order do not show large drops. The dotted line showing the connection between AMC BER switching segments is merely for visualisation of the connection and the measured AMC is the value on the selected fixed-MCS branches. The results should be taken as specified within the abstraction limits. The fixed-MCS receiver is considered a baseline case, as it is the highest end of the spectrum of CSI and knowledge of the ef fective PA linear gain. The PA is memoryless and the goodput does not account for HARQ and control/pilot/scheduling overheads. The simplifications are intentional since the goal is to look at the relative AMC threshold shifts caused by fading statistics and transmitter compression.

6. CONCLUSION

In this paper, a manually decoded LDPC coded SISO-OFDM AMC link has been re-evaluated, with a reproducible finial parameter set and a transparent two-stage method ology. The BER-based thresholds for

MCS are calibrated by using fixed-MCS physical-layer simulations, and are then applied to a Doppler-correlated channel power trace with two-frame delayed and noisy feedback in dynamic AMC. No use of MIESM or any undoc umented SINR/SNDR mapping is used in the revised method.
The quantitative results indicate that the propagation model has a bigger effect on the AMC operating region than the moderate 7 dB-IBO PA setting. The 256-QAM R =2/3 Rician fading is 6.75 dB and 7.00 dB better than the corresponding Rayleigh fading cases, respectively, without and with PA. For Rayleigh fading, that activation is delayed by 1.25 dB by the PA and, for Rician fading, it is delayed by 1.00 dB. All four cases have maximum MCS at 39 dB and goodput values of 41.73 Mbit/s, 39.33 Mbit/s, 44.80 Mbit/s and 44.75 Mbit/s for the Rayleigh/no PA, Rayleigh/PA, Rician/no PA and Rician/PA cases, respectively. Hence, nonlinearity is seen primarily as a change in high-order switching thresholds and mid-SNR goodput, and not as a permanent high-SNR MCS saturation, under the final PA operating point. In future, the perfect CSI assumption can be removed, allowing for pilot-based channel estimation, memory polynomial or Volterra PA models and RF measured data, and the extension of the goodput model to HARQ and practical control/pilot overhead. These extensions would add more realism to the model depending on the threshold calibration framework utilized in this work.

7. REFERENCES

[1] J. G. Proakis and M. Salehi, Digital Communica tions, 5th ed. New York, NY, USA: McGraw-Hill, 2008.
[2] A. Goldsmith, Wireless Communications. Cam bridge, U.K.: Cambridge University Press, 2005.
[3] D. Tse and P. Viswanath, Fundamentals of Wire less Communication. Cambridge, U.K.: Cambridge University Press, 2005.
[4] Y. S. Cho, J. Kim, W. Y. Yang, and C. G. Kang, MIMO-OFDM Wireless Communications with MATLAB. Singapore: Wiley, 2010.
[5] H. Zarrinkoub, Understanding LTE with MATLAB. Hoboken, NJ, USA: Wiley, 2014.
[6] E. Dahlman, S. Parkvall, and J. Skold, 5G NR: The Next Generation Wireless Access Technology. Ams terdam, The Netherlands: Academic Press, 2018.
[7] S. C. Cripps, RF Power Amplifiers for Wireless Communications, 2nd ed. Norwood, MA, USA: Artech House, 2006.
[8] F. M. Ghannouchi, O. Hammi, and M. Helaoui, Be havioral Modeling and Predistortion of Wideband Wireless Transmitters. Hoboken, NJ, USA: Wiley, 2015.
[9] K. Kostrzewska and P. Kryszkiewicz, “Power ampli fier modeling framework for front-end-aware next generation wireless networks,” Electronics, vol. 13, no. 9, p. 1643, 2024.
[10] P. Kryszkiewicz, “Efficiency maximization for battery-powered OFDM transmitter via amplifier operating point adjustment,” 2024.
[11] A. H. Ali, S. S. Hreshee, S. Al-Chlaihawi, F. H. Najjar, and S. H. Abdulwahid, “A developed polar coded generalized frequency division multiplexing based on bit-interleaved coded modulation,” 2024.
[12] H. Hammood, A. H. Ali, and N. J. Aklo, “The ef fect of sample size on the interpolation algorithm of frequency estimation,” Iraqi Journal for Electri cal and Electronic Engineering, vol. 21, no. 1, pp. 156–161, 2025.
[13] K. Sowmya, V. U. Kiran, G. M. Reddy, S. Harika, and K. Siddartha, “Study and analysis of OFDM under Rayleigh fading channel using various mod ulation methods,” Mesopotamian Journal of Com puter Science, pp. 134–142, 2023.
[14] B. Bharadwaja, J. Swagath, E. R. Charan, and V. Sandeep, “Performance analysis of OFDM under Rician fading channel using various digital modu lation methods,” International Journal of Research in Science and Engineering, vol. 3, no. 6, pp. 31–42, 2023.

[15] J. Ketonen, M. Juntti, and J. R. Cavallaro, “Receiver implementation for MIMO-OFDM with AMC and precoding,” in Proc. Asilomar Conf. Sig nals, Systems, and Computers, 2009, pp. 1268 1272.
[16] H. A. Leftah and H. N. Alminshid, “Channel capac ity and performance evaluation of precoded MIMO OFDM system with large-size constellation,” Inter national Journal of Electrical and Computer Engi neering, vol. 9, no. 6, pp. 5024–5030, 2019.
[17] P. N. Kota, A. N. Gaikwad, and P. M. Patil, “Adap tive modulation for SFBC-OFDM systems with zero-forcing equalization,” Communications on Ap plied Electronics, vol. 3, no. 2, pp. 6–11, 2015.
[18] E. C. V. Boas, J. D. S. e Silva, F. A. P. de Figueiredo, L. L. Mendes, and R. A. A. de Souza, “Artificial intelligence for channel estimation in mul ticarrier systems for B5G/6G communications: A survey,” 2024.
[19] W. Hussein, K. Audah, N. K. Noordin, H. Kraiem, A. Flah, M. Fadlee, and A. Ismail, “Least square estimation-based different fast fading channel mod els in MIMO-OFDMsystems,” International Trans actions on Electrical Energy Systems, vol. 2023, p. 5547634, 2023.
[20] A. Gautam, P. Thakur, and G. Singh, “Advanced channel coding schemes for B5G/6G networks: State-of-the-art analysis, research challenges and fu ture directions,” 2024.
[21] M. K. Roberts and A. Parthibaraj, “A comparative review of recent advances in decoding algorithms for low-density parity-check codes and their appli cations,” 2024.
[22] T. Richardson and R. Urbanke, Modern Coding Theory. Cambridge, U.K.: Cambridge University Press, 2008.
[23] C. Tarver, M. Tonnemacher, H. Chen, J. Zhang, and J. R. Cavallaro, “GPU-based LDPC decoding for 5G and beyond,” IEEE Open Journal of Circuits and Systems, vol. 2, pp. 278–290, 2021.
[24] N. Han, I.-M. Kim, and J. So, “Lightweight LSTM based adaptive CQI feedback scheme for IoT de vices,” Sensors, vol. 23, no. 10, p. 4929, 2023.
[25] H. Kim, K. Seol, and J. Kim, “An optimal calibra tion factor for mutual information effective SINR mapping scheme in 5G NR,” 2024.
[26] A. Mazumdar, S. Paris, A. Amiri, K. I. Pedersen, and R. Adeogun, “Enhancing OLLA via exponen tial decay for efficient link adaptation in emerging 6G traffic,” 2024.
[27] A. Mazumdar, A. Amiri, S. Paris, K. I. Pedersen, and R. O. Adeogun, “Enriched HARQ feedback for link adaptation in 6G,” 2024
[28] F. Geiser, D. Wessel, M. Hummert, A. Weber, D. Wubben, A. Dekorsy, and A. Viseras, “DRLLA: Deep reinforcement learning for link adaptation,” 2024.
[29] X. Lu, Q. Zhou, L. Zhu, Z. Wei, Y. Wu, Z. Liu, and Z. Chen, “A low-computational-complexity digital predistortion model for wideband power amplifier,” 2024.
[30] S. Kiambi, E. Mwangi, and G. Kamucha, “Reduc ing PAPR of OFDM signals using a tone reservation method based on $\ell\infty$-norm minimization,” Journal of Electrical Systems and Information Technology, vol. 9, no. 12, 2022.
[31] L. Cho, X. Yu, C.-Y. Hsu, and P.-H. Ho, “Mitiga tion of PA nonlinearity for IEEE 802.11ah power efficient uplink via iterative subcarrier regulariza tion,” IEEE Access, vol. 9, pp. 15659–15669, 2021.
[32] L. Cho and S.-H. Fu, “Generalized Papoulis Gerchberg algorithm for PA nonlinearity compen sation in coded OFDM systems,” 2024.
[33] T. Feys, L. V. der Perre, and F. Rottenberg, “To ward energy-efficient massive MIMO: Graph neural network precoding for mitigating nonlinear PA dis tortion,” IEEE Transactions on Cognitive Commu nications and Networking, 2024.
[34] B. Khan, N. Tervo, M. Jokinen, A. Parssinen, and M. Juntti, “Statistical digital predistortion of 5G millimeter-wave RF beamforming transmitter un der random amplitude variations,” IEEE Transac tions on Microwave Theory and Techniques, vol. 70, no. 9, pp. 4284–4297, 2022.